

Toxic Particles Deposition in the Human Respiratory Tract under Natural Inspiratory Flow

Digamber Singh

Department of Chemical Engineering,
Indian Institute of Technology Kanpur, Kanpur, Uttar Pradesh, India.
Corresponding author: digamber35@gmail.com

Bholu Kumar

Department of Mechanical Engineering,
Poornima University Jaipur, Jaipur, Rajasthan, India.
E-mail: bholu.kumar@poornima.edu.in

Anuj Jain

Department of Applied Mechanics,
Motilal Nehru National Institute of Technology Prayagraj, Prayagraj, Uttar Pradesh India.
E-mail: anujjain@mnnit.ac.in

Akshoy Ranjan Paul

Department of Applied Mechanics,
Motilal Nehru National Institute of Technology Prayagraj, Prayagraj, Uttar Pradesh India.
E-mail: arpaul@mnnit.ac.in

(Received on July 16, 2023; Accepted on October 6, 2023)

Abstract

Toxic particle ($PM_{2.5}$) deposition in the human respiratory tract is investigated under natural inspiratory flow. The flow physics of nostrils is asymmetric, and its effect on particle deposition needs prompt attention. An ideal 3-D CT-scan-based geometrical model of the human respiratory tract is re-constructed from the nasal cavity to the 7th generation bronchi. The pulsatile numerical simulation is performed with light (10 L/min) and moderate (40 L/min) inspiratory flow. The Lagrangian method is adopted to compute particle deposition fraction (DPF) in the airways. The suspended particle mass of $300 \mu\text{g}/\text{m}^3$ (poor air quality) ($d_p = 2.5 \mu\text{m}$ in diameter) is released from the inlet of airways at every time interval (Δt). The results revealed that the pattern of particle transportation is not similar in both the bronchus and particle hot spots are constituted in the airways. Findings guide optimal targeted drug delivery and the assessment of ventilation illness under hazardous exposure in distinct populations.

Keywords- Human respiratory tract (HRT), Computed tomography (CT), Air quality index (AQI), Particulate matter (PM), Discrete phase model (DPM), Numerical simulation.

1. Introduction

The study shows the pulsatile asymmetric inflow characteristics and toxic air pollutants deposition in the human respiratory tract, and the findings reveal fruitful insights for medical practitioners. Thus, due to rapid industrialization and uncontrolled demand for material goods, breathing air quality is decreasing significantly. Which can constitute breathing disorders, as discussed by Tanprasert et al. (2023).

The deposition of micro-size particles has imposed a huge burden of mortality loss (3.17 million) worldwide in the year 2015, as per a WHO (World Health Organization) report. It is also smashing the quality of human lives, and it increases the burden of mortality loss (Mathers et al., 2006). Therefore, mortality due to respiratory illness will be the fourth largest cause in the world by 2030. These issues are

investigated under natural inspiratory flow conditions. Furthermore, Deng et al. (2019) found particle deposition was strongly affected by physical activities due to different inspiratory flow rates, which need prompt attention. The concentration of PM_{2.5} particles in the air throughout the year is changing. In the months of October to January, the concentration was very poor. Also, significant changes were observed in PM_{2.5} particle density from year to year. It also increases the burden of severe diseases in middle and low income countries.

The nasal cavity has a complex anatomy with several irregularities. Consistently, a high velocity magnitude was observed in the nasal valve. As the inspired air reaches a conditioned state in the middle region of the nasal cavity, Additionally, very low air volume is passed from the nasal valve to the olfactory region (Inthavong et al., 2018). Also, airflow in the nasal cavity exhibits a sharp gradient of flow. Therefore, dense mesh was constructed near the flow wall, which can capture the flow physics of the wall (Inthavong et al., 2019).

Zhang et al. (2001) showed the sixth-generation human airways model's oscillatory flow and particle deposition results. He obtained the coherent structure of fine particles while breathing in the human airway. He showed variation in the secondary flow vortices at the bifurcated junction. However, during heavy breathing, the upper airways were turbulenced in the larynx due to the momentum of the flow. Also, Lin et al. (2007) presented the impact of induced turbulence by the laryngeal jet on airflow patterns and tracheal wall shear stress. A recent study was conducted by Shrivastav et al. (2019). The turbulent flow in the human respiratory tract is formed by moderate breathing. The turbulent flow has a large flow velocity gradient near the flow wall. The correct y^+ value is essential for wall-bounded flows.

The natural breathing and CT-scan-based human airways model significantly affects tracheal flow and flow in the first bifurcation junction, which is highly asymmetric due to the cross-section of the bronchus. Thus, the flow is sensitive to the local attributes of the real anatomy (Banko et al., 2016; Luo et al., 2004; and Ma et al., 2018). However, the loss of pressure was not significant in the simplified airway model at the bifurcation junctions (Kang et al., 2011). Besides, flow in the bronchial tube was laminar (Soni and Aliabadi, 2013), and wall shear stress is low in magnitude (0.30 Pa), which is relevant to human health worldwide (Sul et al., 2014).

Kim and Lee (2007) did the experiment to study the laminar flow field through digital micro holographic particle tracking velocimetry in a curved micro-tube with a circular cross-section. He found that there was too low magnitude of flow. The secondary flow vortex was not formed in the curve tube, whereas at high magnitudes of flow, a large-scale counter-rotating flow vortice is observed. Therefore, the respiration profile has significant importance in breathing. Also, the mainstream of flow is asymmetric in nature, and it showed skewed and double-peaked M-shaped patterns (Zhu et al., 2019).

The toxic particle deposition in the HRT model was the main concern for human health. The higher AQI may affect the bed's atmospheric condition during breathing, which might create health diseases (Liu et al., 2015). Piglione et al. (2012) studied the micro-particle deposition phenomena in the tracheobronchial airway. The conductive zone of the lung retained 1, 2, and 10 microns size particles in diameter. The size of the particles moved towards the right branch of the airways beside the left branch, and very few particles crossed the conductive zone of the airway (Gorji et al., 2015). The unsteady airflow is the predicted deposition fraction in a specific region of the human airways. Therefore, the complete HRT model must be used for the study (Naseri et al., 2017). Inter-subject variability and airflow rate had a significant influence on drug delivery and airborne toxic particle deposition (Feng et al., 2018; Huang et al., 2021). The tracheobronchial airways model has complex flow vortices, which heavily affect the

deposition of aerosol particles ($PM_{2.5}$) in the human airways.

Mutuku and Chen (2018) found the mass flow rate in healthy human airways is 3.10 times higher than in diseased (chronic obstructive pulmonary disease) airways. Under a higher flow rate, more particles accumulate in the lower airway regions (Piemjaiswang et al., 2019). Moreover, aerosol deposition is used to cure certain airway diseases, and breathing frequency is having a significant effect on particle deposition (Piemjaiswang et al., 2019).

Despite these and several other related studies, the toxic particle deposition in the human respiratory tract under natural airflow in a 3D *in-silico* model has not been investigated yet, to the best of our knowledge. Therefore, this study has novelties in terms of the adopted boundary conditions and the 7th generation *in-silico* human airway model. We have performed pulsatile simulations in the patient-specific HRT model, and the particle deposition is characterized by a discrete phase model (DPM). The details of respiration characteristics and particle deposition are described in the 7th generation HRT model with noval boundary conditions. Results are reported in the form of net velocity streamlines, axial velocity profiles, secondary flow vortices, pressure profiles, pharynx and larynx jet, particle transport patterns, and deposition fraction. Most of the results are shown in different regions, each corresponding to a specific location. This article provides novel insights to medical practitioners during diagnosis and correlates the pathological aspects of breathing illness.

2. Numerical Methodology

2.1 Human Airways Model and Grid Generation

The two standard methods (CT-scan and simplified modelling) were used to reconstruct the patient-specific CT-scan-based HRT model (Singh et al., 2022). The *in-silico* airway model results were more realistic than the simplified model (Comer et al., 2000). However, it requires more computational effort (Luo et al., 2004). Therefore, it is more important to address the respiratory illness due to poor air quality, which needs to be more sensible to assist the simplified model up to the clinical level (Lopez and Mathers, 2006). The CT-scan-based 3D geometrical model was reconstructed, as shown in Figure 1. The computed tomography technique (CT) was found suitable to detect tissue structure clearly. 1024 two-dimensional CT-scan slices with a field view of 31.60 cm are grown exponentially up to 0.623 mm, and these CT-scan slices are imported into medical imaging software (Sim Viscular). A mask over the segmented images has a Hounsfield Unit (HU) between -1024 and -200. The shown 3D HRT model has 0.0141 and 0.0126 m left and right external nostril hydraulic diameters, respectively. For further processing, a 3D model was imported into ICEM software.

The polyhedral grid cells were comprised inside the complete flow domain shown in Figure 2. Polyhedral element mesh is less sensitive against the starching of elements and provides a flow velocity gradient near the wall (Inthavong et al., 2018; Shang et al., 2019). It shows better performance (convergence) over the tetrahedral grid cells. To minimize the skewness at the sharp corner inside the nasal cavity (Spiegel et al., 2011) and to maintain the appropriate y^+ factor near the wall, ten prism layers were constructed. The grid independence test was performed. To verify grid adequacy by comparing the radial velocity profile at the glottis cross-section shown in Figure 3, the average velocity had <1% differences for an increasing grid size of 68, 90,000 to 89, and 37,979 elements for 4 mm and 3.5 mm elements, respectively. This shows that the 4 mm element size grid is enough for further analysis in this study.

LBUL-Left bronchus upper lung; RBUL-Right bronchus upper lung; LBML-Left bronchus middle lung; RBML-Right bronchus middle lung; LBLL-Left bronchus lower lungs; and RBLL-Right bronchus lower lungs.

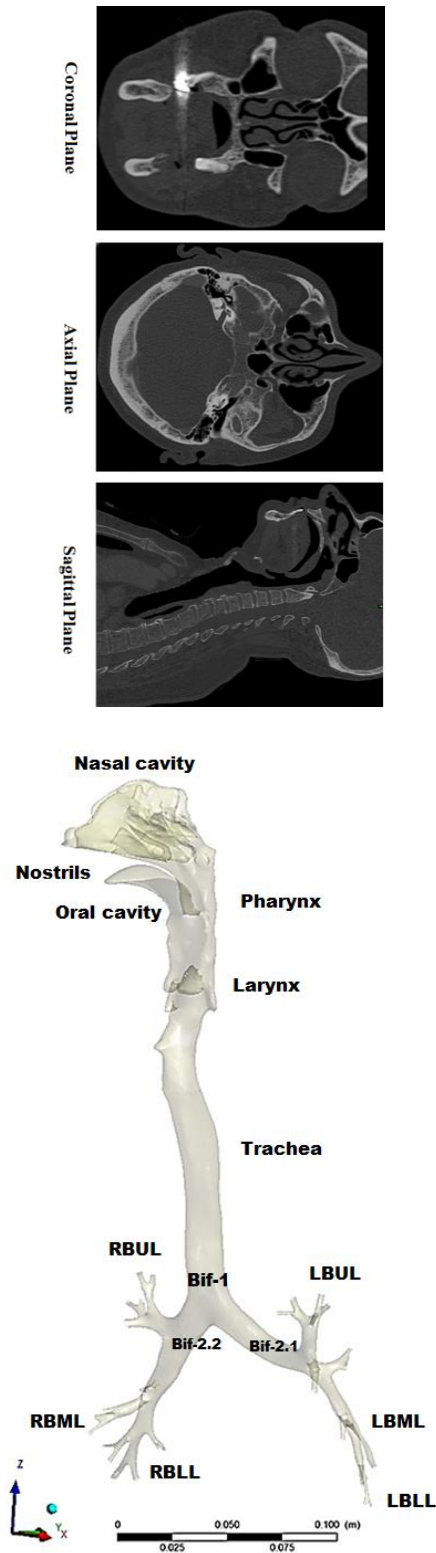


Figure 1. Human airways model nasal cavity to 7th generation bronchi.

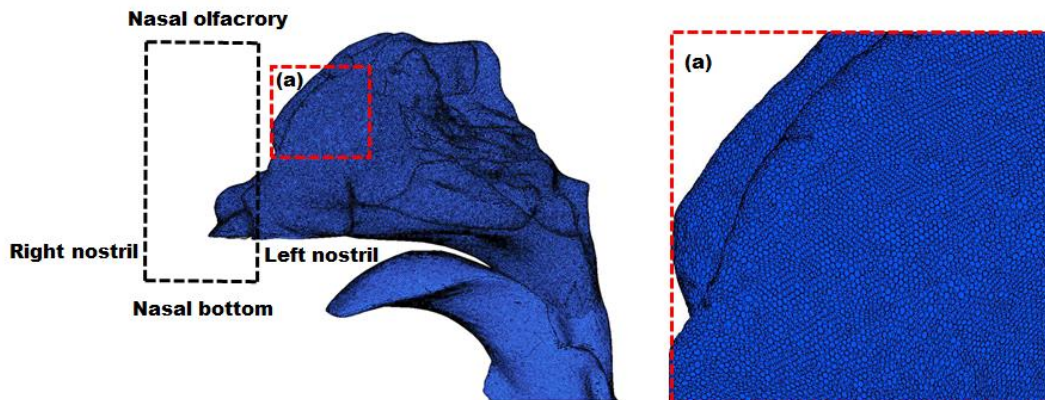


Figure 2. A numerical grid of human respiratory tract model.

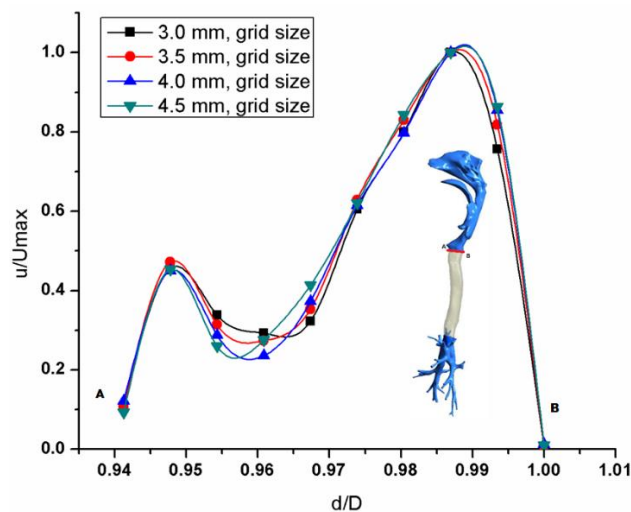


Figure 3. Radial local velocity profile at airway glottis cross-section.

2.2 Initial Boundary Conditions

Two succeeding pulsatile breath profiles Q_{in} , 10 L/min. and 40 L/min are simulated. A user-defined function (UDF) of half period of breath profile shown in Figure 4 is used as a velocity inlet at both nostrils. Results of inspiratory airflow are presented at an interval of $t = 1.0s$ to decrease the effect of initial conditions. The natural breathing is not precisely sinusoidal or symmetric from both nostrils mainly in high breathing (Lee et al., 2010; Naseri et al., 2017; and Singh, 2021). Here, in the present study, the asymmetric pulsatile airflow boundary conditions are considered.

For particle deposition, trap boundary conditions are set up on the airway wall and the Dirichlet boundary condition for pressure is imposed at all outlets of bronchial tubes. The flow wall boundary is considered hydraulically rigid. To maintain the flow sensitivity times step size (Δt) 0.01 is considered. The adaptive time method is used in this study. It keeps on changing up-to order of 10^{-5} (Calmet et al., 2018).

In earlier studies, different micro-size particles were injected in the nostrils without considering ambient

AQI. Which is not a precisely right method. In the present study, $PM_{2.5}$ particle size is injected at each time interval (Naseri et al., 2017) with $AQI\ 300\ \mu\text{g}/\text{m}^3$ during inspiratory airflow. The human respiratory anatomy has mucous membranes, which trap the inspired particles.

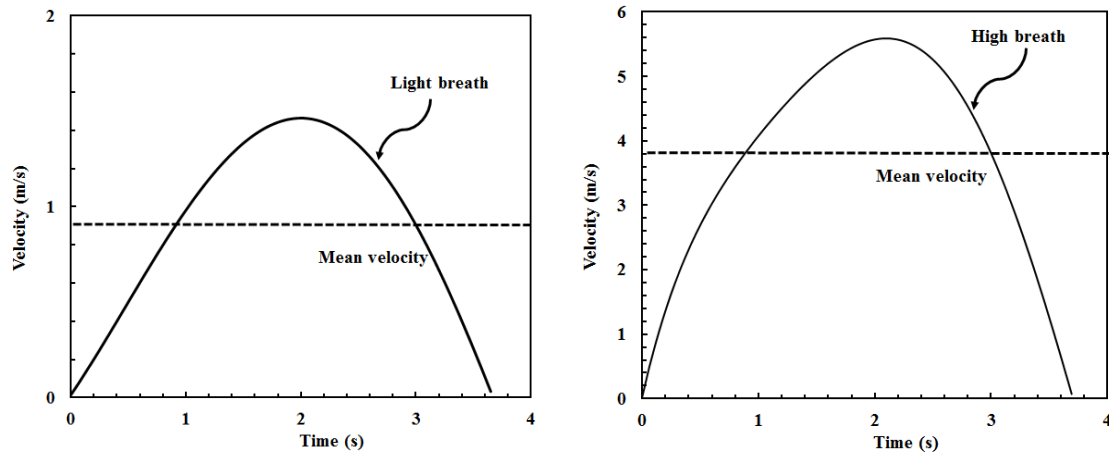


Figure 4. Inspiratory waveform velocity input for breathing conditions (a) light (10 L/min.), and (b) high airflow (40 L/min.).

2.3 Governing Equations and Turbulence Model

The internal dynamics of air within the HRT model are simulated using a finite-volume CFD solver by solving Navier-Stokes mass, and momentum equations, Equation (1) and (2). Additionally, to simulate the 2.5 micro-size particle trajectory inside the human airways discrete phase modelling (DPM) is considered and Equation (8) solve (Gorji et al., 2015; Luo and Liu, 2009; Pigiione et al., 2012; and Zhang and Kleinstreuer, 2002).

The continuity and momentum equations are given below;

Continuity equation:

$$\frac{\partial(\rho u_i)}{\partial x_i} = 0 \quad (1)$$

Momentum equation:

$$\frac{\partial u_i}{\partial t} + \frac{\partial(u_i u_j)}{\partial x_j} = -\frac{1}{\rho} \frac{\partial p}{\partial x_i} + \frac{\mu}{\rho} \frac{\partial^2 u_i}{\partial x_j \partial x_j} \quad (2)$$

where, u_i and u_j ($i, j = 1, 2, 3$) are the velocity components of inspired airflow in x , y and z directions.
 p = static pressure (Pa), ρ = density of fluid ($1.225\ \text{kg}/\text{m}^3$).

2.4 Turbulence Models

2.4.1 Realizable k - ε Turbulence Model

The k - ε turbulence model has good agreement with the flow separation, boundary layer under adverse pressure gradients, and flow recirculation (Ansys fluent guide, 2016; Srivastav et al., 2019), and the enhanced wall function is used with a curvature correction factor.

The transport equations for the k (turbulent kinetic energy) ε (turbulent dissipation rate) model are below.
 k – equation,

$$\frac{\partial}{\partial t}(\rho k) + \frac{\partial}{\partial x_j}(\rho k u_j) = \frac{\partial}{\partial x_j} \left[\left(\mu + \frac{\mu_t}{\sigma_k} \right) \right] + G_k + G_b - \rho \varepsilon - Y_M + S_k \quad (3)$$

ε -equation

$$\frac{\partial}{\partial t}(\rho \varepsilon) + \frac{\partial}{\partial x_j}(\rho \varepsilon u_j) = \frac{\partial}{\partial x_j} \left[\left(\mu + \frac{\mu_t}{\sigma_\varepsilon} \right) \right] + \rho C_1 S_\varepsilon - \rho C_2 \frac{\varepsilon^2}{k + \sqrt{v \varepsilon}} + C_{1\varepsilon} \frac{\varepsilon}{k} C_{3\varepsilon} G_b + S_\varepsilon \quad (4)$$

where, model, $C_1 = \max \left[0.43, \frac{\eta}{\eta + 5} \right]$, $C_2 = 1.9$, and $C_\mu = 0.09$ are constants.

$\eta = S \frac{k}{\varepsilon}$ where, S is the module of the mean rate of strain tensor are stated as, $S = \sqrt{2 S_{ij} S_{ij}}$.

Turbulent/eddy viscosity is defined as, $\mu_t = \rho C_\mu \frac{k^2}{\varepsilon}$.

Turbulence kinetic energy due to the mean velocity gradients = G_k .

Turbulence kinetic energy due to buoyancy = G_b .

Fluctuating dilatation incompressible turbulence to the overall dissipation rate = Y_M .

The model constant $C_2 = 1.9$, and $C_{1\varepsilon} = 1.44$, are model constants.

S_k and S_ε are user-defined source term, which equals to zero.

Turbulent Prandtl number for k , $\sigma_k = 1$.

Turbulent Prandtl number for ε , $\sigma_\varepsilon = 1.2$.

2.4.2 Low Reynolds Number (LRN) k - ω Turbulence Model

The LRN k - ω model was found relatively better to compute the mixed turbulence inside the human airways (Gorji et al., 2015; Srivastav et al., 2019).

The transport equations for, k (turbulent kinetic energy) and ω (specific turbulent dissipation rate) models are described below.

k - equation

$$\frac{\partial k}{\partial t} + u_j \frac{\partial k}{\partial x_j} = \tau_{ij} \frac{\partial \bar{u}_j}{\partial x_j} - \beta^* k \omega + \frac{\partial}{\partial x_j} \left[(v + \sigma_k v_T) \frac{\partial k}{\partial x_j} \right] \quad (5)$$

ω - equation

$$\frac{\partial \omega}{\partial t} + u_j \frac{\partial \omega}{\partial x_j} = \alpha \frac{\omega}{k} \tau_{ij} \frac{\partial \bar{u}_j}{\partial x_j} - \beta \omega^2 + \frac{\partial}{\partial x_j} \left[(v + \sigma_\omega v_T) \frac{\partial \omega}{\partial x_j} \right] \quad (6)$$

where, v , v_T and τ_{ij} are the kinetic molecular viscosity, turbulence viscosity of fluid and Reynolds stress tensor. The turbulence viscosity of the fluid states as $v_T = C_\mu f_\mu k / \omega$.

$$f_\mu = \exp \left[\frac{-3.4}{(I - R_T)^2} \right] \quad (7)$$

Here, $R_T = \left(\frac{k}{\mu\omega} \right)$ and μ are molecular dynamic viscosity of the fluid. The model constants value are $C_\mu = 0.09$, $\alpha = 0.555$, $\beta = 0.8333$, $\beta^* = 1$, and $\sigma_k = \sigma_\omega = 0.5$.

2.4.3 Discrete Phase Model (DPM)

The inspiratory flow is a mixture of air and micro-sized particles. Which is inducted either naturally or by other external sources such as inhalers and cigarette smoking. For the two-phase coupling of air and particles, a discrete phase model (DPM) was used. The DPM is used to simulate different types of two-phase flows such as aerosol dispersion, bubble sparing of liquids, and particle analysis (Gorji et al., 2015; Pirhadi et al., 2018; Srivastav et al., 2014). Lagrange force balance Equation (8) is used to compute the trajectory of inspired particles.

Equation (8) equates the particle inertia with the forces acting on the injected particle and state (for the x-direction in Cartesian coordinates) as,

$$\frac{du_p}{dt} = F_D(u - u_p) + \frac{g_x(\rho_p - \rho)}{\rho_p} + F_x \quad (8)$$

where, $F_D(u - u_p)$ and g_x are the drag force (drag force is a function of the relative velocity) particle mass and represents the gravity.

$$F_D = \frac{18\mu}{\rho_p d_p^2} \frac{C_D \text{Re}}{24} \quad (9)$$

Here, u is the airflow velocity, u_p is the injected particle velocity, ρ_p is the density of micro-size particles and d_p is the particle diameter. Re is the relative Reynolds number, which is defined as,

$$\text{Re} = \frac{\rho d_p |u_p - u|}{\mu} \quad (10)$$

The drag coefficient, C_D , can be written as,

$$C_D = a_1 + \frac{a_2}{\text{Re}} + \frac{a_3}{\text{Re}^2} \quad (11)$$

where a_1 , a_2 , and a_3 are constants (Morsi and Alexander, 1972).

2.5 Numerical Simulation

The SIMPLE-C scheme is used for pressure-velocity coupling (Mutuku et al., 2018; Yang et al., 2006). The transport equations Equation (1) and (2) were discretized using second-order schemes in space and the second-order QUICK (Quadratic Upstream Interpolation for Convective Kinematics) scheme was used (Srivastav et al., 2019) for the convective term. The central difference scheme is considered for diffusion terms with a relaxation factor of 0.1. To compute the flow phenomena near the boundary wall y^+ (Y-plus) was defined as local Reynolds number ($Re_e = \rho u D / \mu$). y^+ is used to agree to the quality of mesh near the flow boundary (Salim and Cheah, 2009; Srivastav et al., 2019).

The adaptive time method was used (Kleinstreuer and Zhang, 2002) and the numerical solution was converged up to 10^{-5} residual in scale (Mutuku et al., 2018). 2.5-micron-sized solid particles were injected

at the inlet of both nostrils and followed at every interval, and deposition of particles occurred as the particles touched the wall. Flow coupling is considered in this study (Gorji et al., 2015; Huang et al., 2021) and the properties of the particles include, particle density (ρ) 1000 kg/m³, the shape of particles assumed to be spherical, construction of PM_{2.5} in the air (AQI) 300 µg/m³, and the injection of particles followed the inlet velocity of air (Luo and Lin, 2009).

2.6 Computation Validation

2.6.1 Airflow

The nasal cavity airflow pattern disclosed the nozzle effect at the entry of the nose, due to the contraction of the cross-section area. The maximum static pressure drop occurs in that region. Figure 5 shows the average static pressure drop (Δp) at the nasal valve (slice-1) under different inspiratory flow rates. The computed results of the airflow pattern in the nasal cavity have confirmed the nature of breathing.

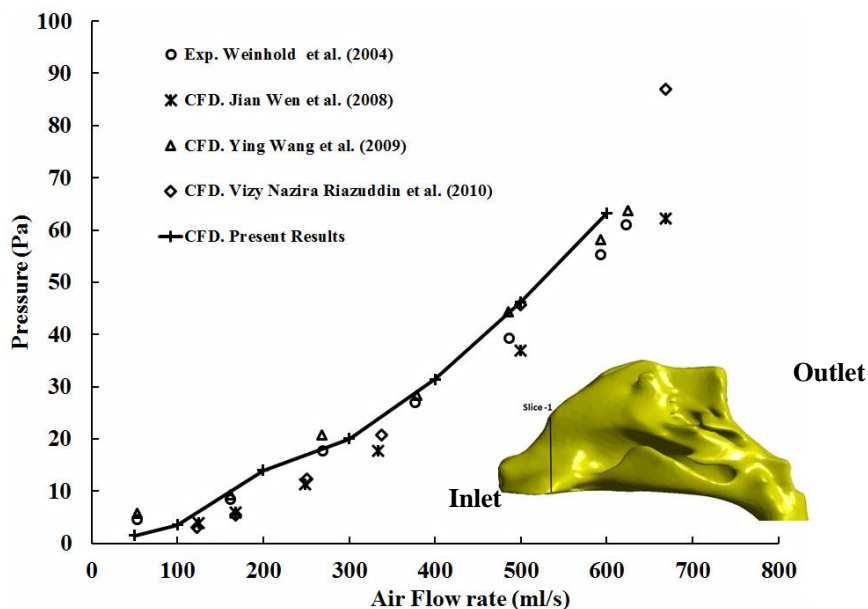


Figure 5. A comparison of pressure (Pa) during inspiratory airflow at the nasal valve region with the experimental and simulation results (Riazuddin et al., 2011; Wang et al., 2009; Weinhold and Mlynski, 2004; Wen et al., 2008).

The computational results are agreed with the experimental and computational results showed by Riazuddin et al. (2011), Wang et al. (2009), Weinhold and Mlynski (2004), Wen et al. (2008). A similar human respiratory model is mimicked from CT-scan slices discussed in section 2.1. The constant inlet velocity conditions are imposed at both nostrils for various mass flow rates. The results are compared with experimental and simulation results presented in the literature.

2.6.2 Different Micro-size Inspired Particles

In Figure 6, the particle deposition efficiency is evaluated during 30 L/min inspiratory flow with 1 to 10 micro-size particles in the nasal cavity. The deposition efficiency is computed from Equation (12). Where DE is the deposition efficiency, and P_{out} is the concentration of escaped particles measured at the outlet of the nasal cavity, and P_{in} is the concentration of injected of different micro-sizes particles at the inlet of the nasal cavity.

$$DE = 1 - \frac{P_{out}}{P_{in}} \quad (12)$$

The characteristics effects of dp and Q are interlinked to each other. The different types of geometrical models were chosen such as SLA and Viper (anatomical model surface smoothness). With the internal rough surfaces, numerical results closely match with Kelly et al. (2004) and confirmed by Schroeter et al. (2011). Kelly et al. (2004) showed micro-particle deposition in the nasal cavity and compared it with steady-state simulated results. A similar method was adopted by Gorji et al. (2015). Therefore inspiratory airflow and micro-particle DE are evaluated during steady-state flow conditions, and simulated results are compared with the experimental data, and it has a good match.

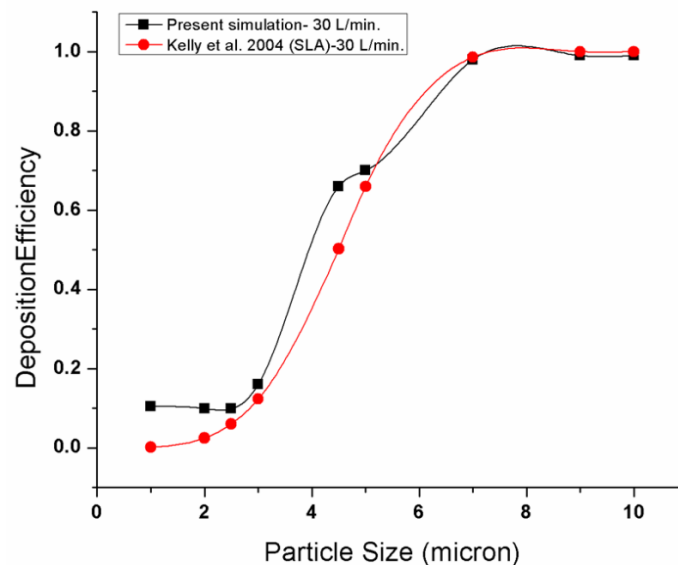


Figure 6. A comparison of predicted inspired different micro-size particles deposition in the nasal cavity with the experimental data (Kelly et al., 2004).

3. Results and Discussion

The toxic particle deposition and hydrodynamic characteristics in the human respiratory tract are studied. The transient numerical simulations were performed under natural inspiratory flow (10 and 40 L/min). The numerical results are presented at different time steps and discussed in the following sections.

3.1 Asymmetry in the Nasal Cavity Flow

The velocity streamlines color contours are shown in Figure 7 and it shows the flow pattern in the nasal cavity.

As the air enters in the nasal cavity, the high flow velocity (3.0 m/s) is observed in the nasal valve region. However, at the nasal valve, the flow velocity increases under moderate breathing up to 10.0 m/s shown in Figure 7 at $t = 2.07s$. The nasal cavity has a nozzle effect in that region due to the contraction of the cross-section. Furthermore, the flow propagates through the nasal turbinate region and the asymmetry in nostrils flow is disclosed. The mean velocity profiles are reported in the human upper airway region

(marked in Figure 8(a) and shown in Figure 8(b)). It shows significant differences in flow velocity distribution in both nostrils (Keyhani et al., 1995). The left cavity of the nasal has higher flow velocity as evidenced by the colour contours and mean velocity profiles.

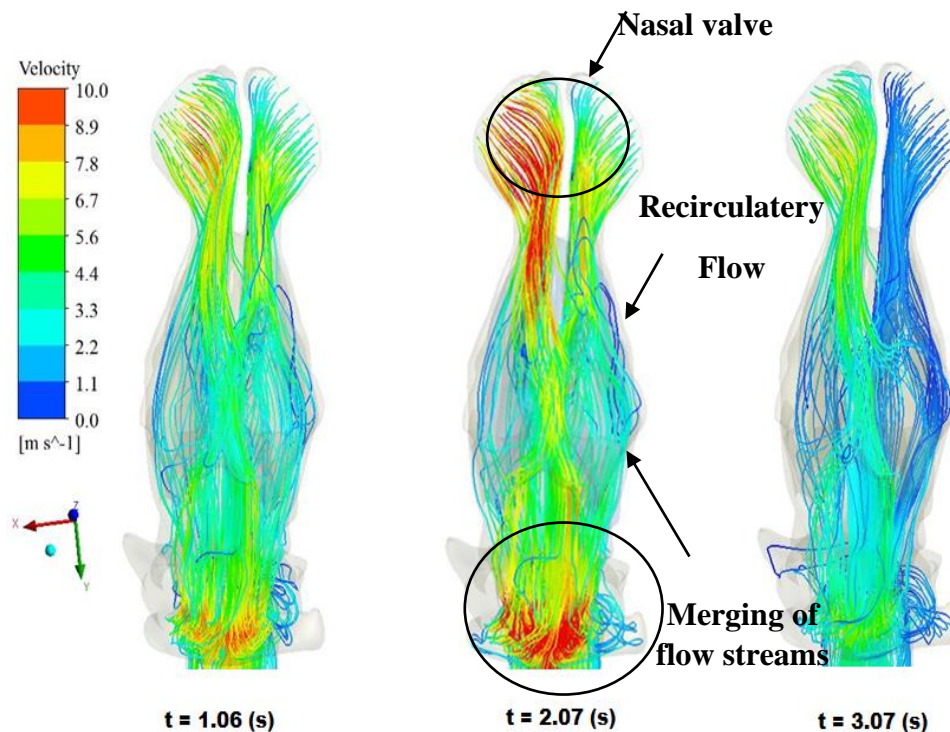
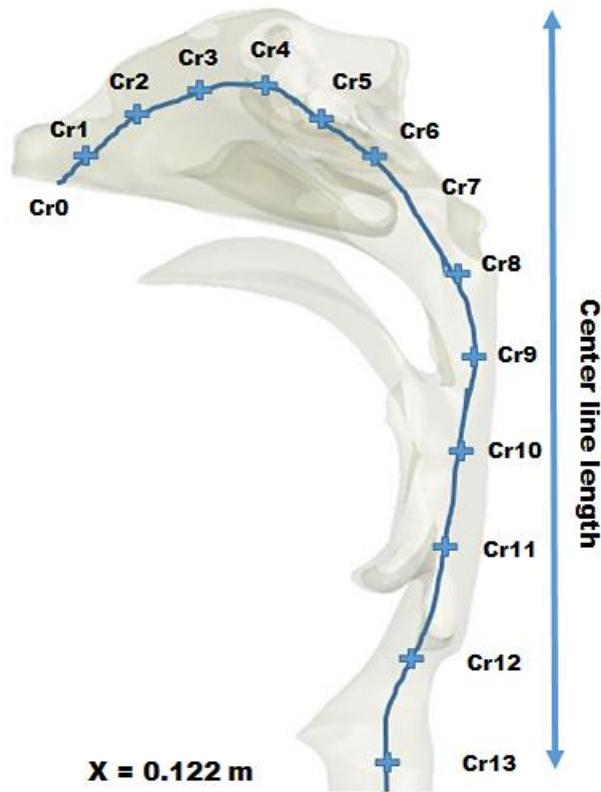


Figure 7. Transient streamlines airflow in the nasal cavities, under the flow rate (10 L/min).

In the respiratory region, recirculatory flow occurs around the turbinate region, marked by the arrow in Figure 7. However, the recirculatory flow in the right cavity is prominently higher as compared to the left cavity, and it is increasing under the low magnitude of the flow. Due to the reduction in the cross-sectional area of the nasal valve, the palate (bottom of the nasal cavity) and olfactory region receive less low-flow velocity volume of air. This is evident from the colour contours and the recirculatory flow present in that region (Shang et al., 2019).

The asymmetricity in nasal cavity flow has disappeared in the pharynx and larynx regions. Due to the merging of flow streams in the nasopharynx region shown in Figure 7 (marked with a circle), the velocity profiles are computed at different time step sizes, as shown in Figure 9. Similar trends of results are observed under a high inspiratory flow rate (40 L/min). The numerical findings revealed the asymmetricity in nasal cavity flow, which disappeared in the lower airways.



Cr- cross-section of marked location.
(a)

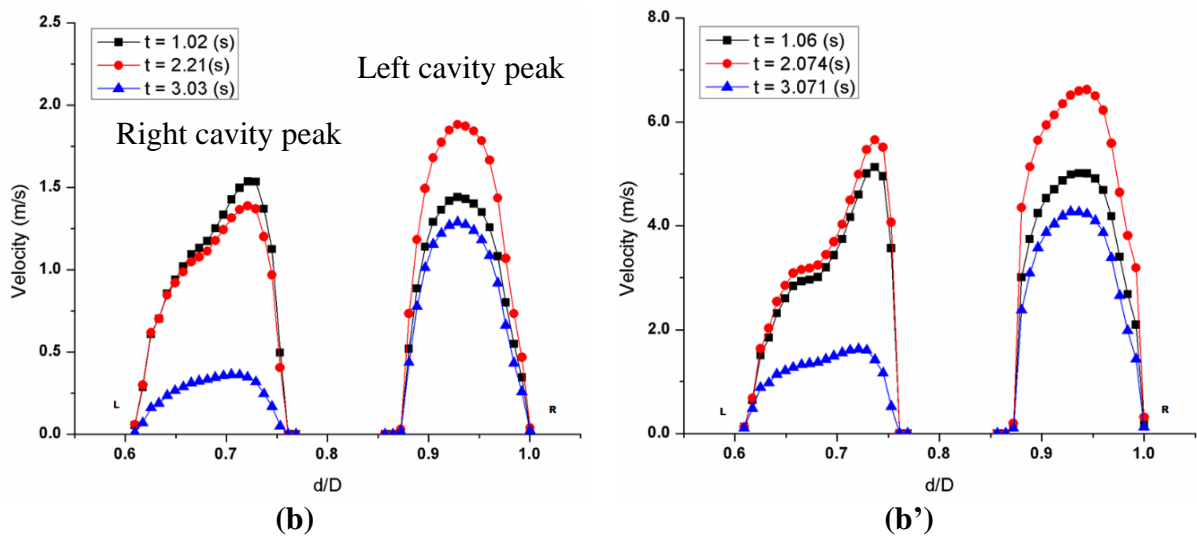


Figure 8. (a) CT-scan based human upper airways model. (b) Mean airflow velocity profile at nasal valve under the flow rate of, (b) 10 L/min, and (b') 40 L/min.

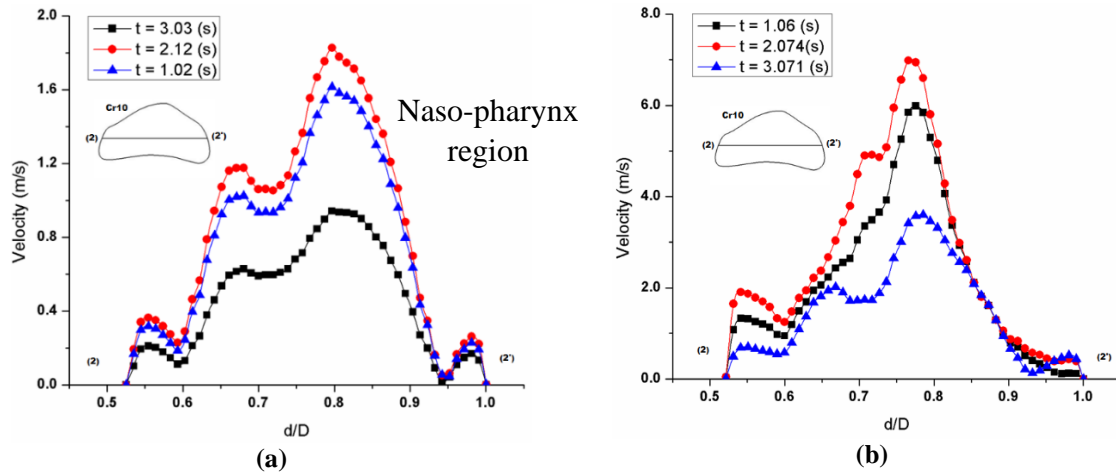


Figure 9. Mean velocity profile at the naso-pharynx region of human airways, under the flow rate of, (a) 10 L/min, and (b) 40 L/min.

3.2 Secondary Flow Vortices

In Figure 10, the velocity color contours and flow streamlines are presented at the entry of respiration through vertical plane bb.

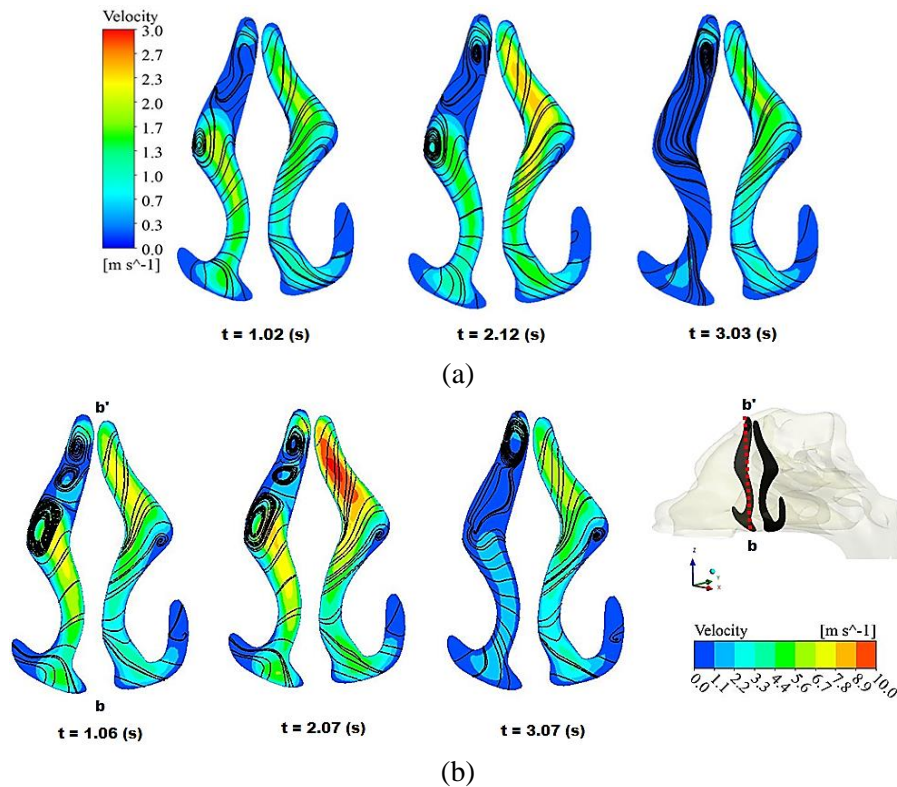


Figure 10. Secondary flow streamlines and velocity contours at the entry of the respiration region, under the flow rate of (a) 10 L/min, and (b) 40 L/min.

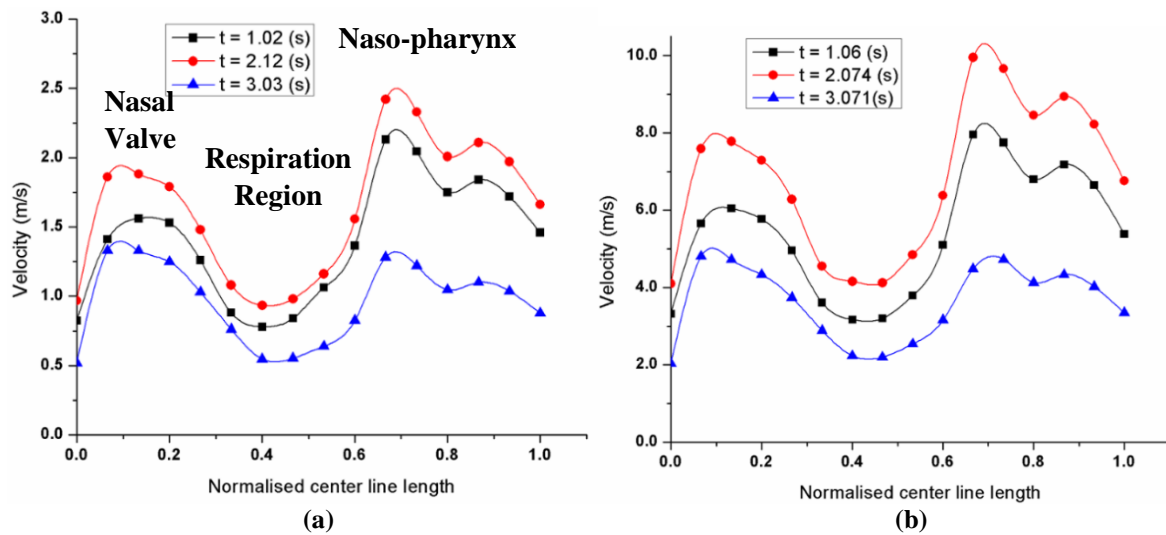


Figure 11. Mean velocity profile in the Human Upper Airways, under the flow rate of, (a) 10 L/min, and (b) 40 L/min.

The results showed the right cavity has flow vortices in the middle and upper turbinate regions. In contrast, the higher velocity is observed in the upper turbinate under peak inspiratory flow ($t = 2.07$ s) in Figure 7. The length scale of vortices is decreasing with respect to space and velocity magnitude, as shown in Figure 7 ($t = 3.07$ s). It is expected that under moderate breathing (40 L/min), the flow velocity magnitude is increasing, and three vortices are shown in the right nasal cavity with one vortex in the left cavity ($t = 2.07$ s). Also, the higher velocity magnitude (10 m/s) occurred in the upper turbinate of the left cavity. It is the character of the airways narrowed cross-section, and the velocity's magnitude is reduced.

In Figure 10(b) at $t = 3.07$ s the upper turbinate vortices are combined together due to the low-velocity magnitude. Similarly, the mean velocity profiles are presented at different time steps for both flow rates shown in Figure 11(a) & (b). It shows the variation in flow velocity magnitude inside the nasal cavity. Results showed high flow vortices in the right nasal cavity at the middle and upper turbinate region, and it is increasing under moderate breathing, which may increase a sense of smell and particle deposition.

In Figures 12(a) and (b), velocity flow streamlines color contours in the pharynx, larynx, and trachea at different cross-sections are presented. Due to the merging of flow streams at the nasopharynx, the directional (x-direction) flow is accelerated because of the 90° bend of the nasopharynx. Thus, a sharp jet of flow occurred (Lin et al., 2007) in the pharynx and larynx regions shown in Figure 13 under normal and high inspiratory flow rates, which affects the main stream of flow in the tracheal.

Under moderate flow rate (40 L/min) at $t = 2.07$ s, the maximum velocity of 8.0 m/s is obtained and seen in the pharynx and larynx region. The flow jet is attached to the posterior wall of the airway. The flow separation and secondary flow vortices are depicted along the anterior wall. It is evident from the color contour at $t = 2.12$ s under normal inspiratory flow. The flow jet significantly influences particle deposition (Shang et al., 2019).

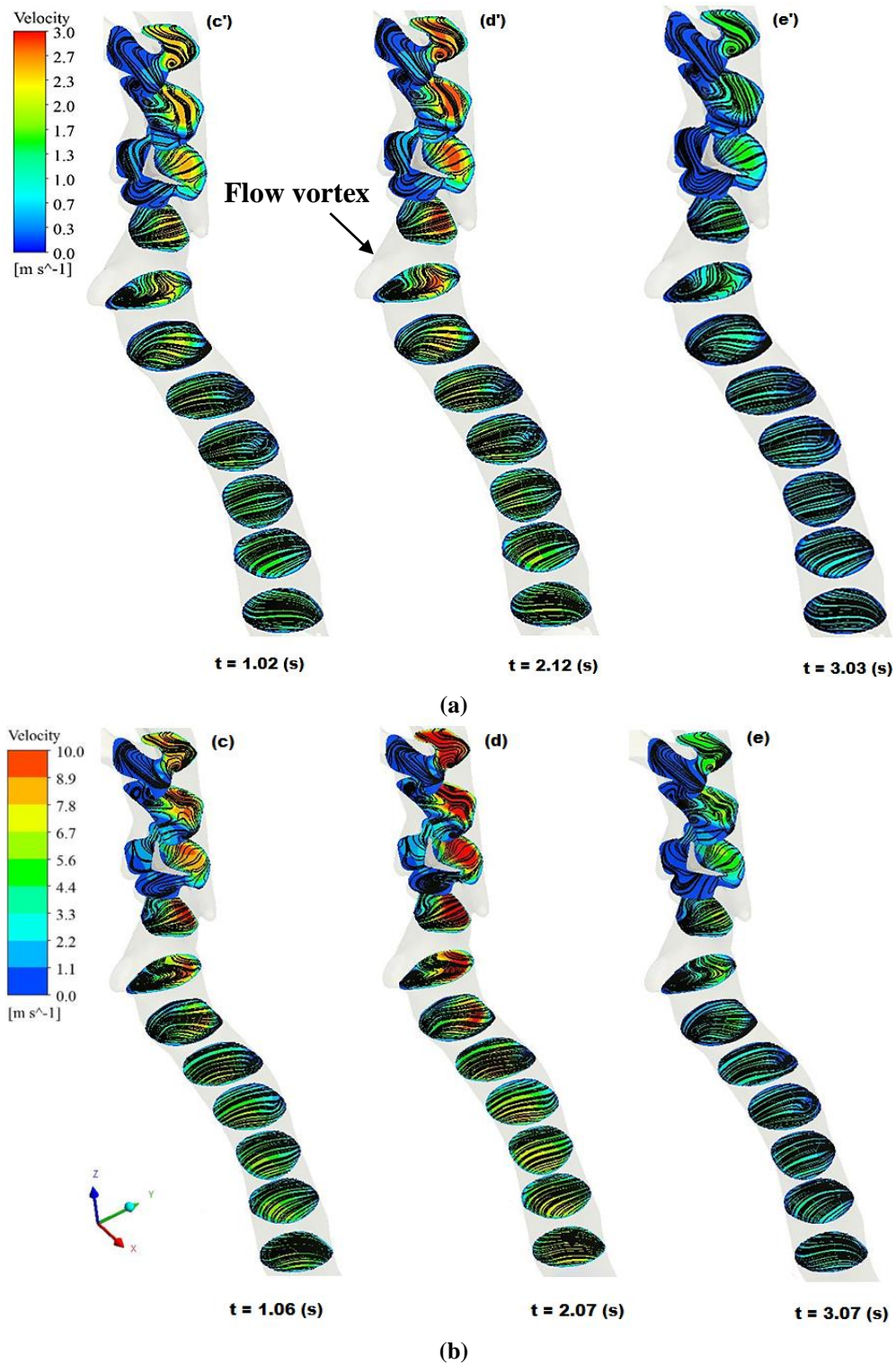


Figure 12. Secondary flow streamlines and velocity contours in pharynx, larynx and trachea region, under the flow rate of, (a) 10 L/min, and (b) 40 L/min.

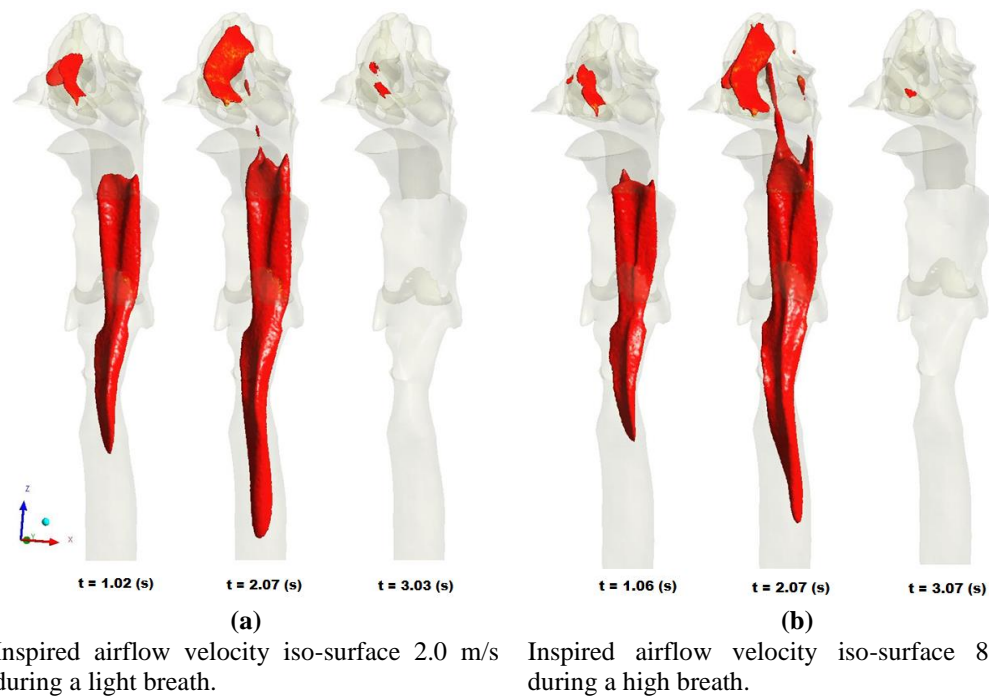
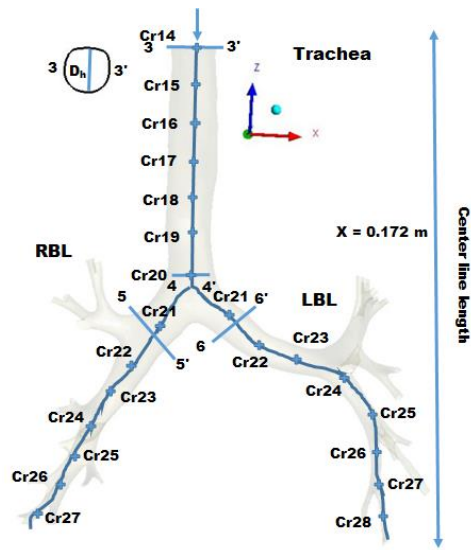


Figure 13. The laryngeal jet region in the upper airways, under the flow rate of, (a) 10 L/min, and (b) 40 L/min.

The pulsatile airflow undergoes a significant variation in velocity magnitude and secondary flow vortices in the pharynx. Thus, the multiple flow vortices show flow separation and recirculation of flow due to the anatomical structure of the airway. Moreover, the larynx surface bend passed the maximum mass of flow along the anterior side, and the color contours showed the maximum magnitude of velocity constituted along the posterior side of the pharyngeal wall. At the entry of the trachea, a single flow vortex is observed along the anterior side, marked in Figure 12(a) at $t = 2.12$ s. The length scale of the flow vortex decreases as flow velocity decreases ($t = 3.03$ s).

Furthermore, flow progressed in the trachea. The magnitude velocity is reduced because of the cross-sectional area. The flow vortices are along the posterior wall. However, the streamlined patterns are presented at two inhalation flow rates. In Figure 14, the tracheobronchial airways tree shows the marked locations of numerical results. The velocity profile in the tracheobronchial tree at different locations (Cr20 and 21) is shown in Figure 15 under normal and high flow rates at different time steps. Which includes all flow features of anatomical airways. At the cross-section Cr20, the velocity significantly affects the zeroth junction of the laryngeal jet in both conditions. It is evident from the color contours in Figures 12 (a) and (b).

The flow stream is moved towards the posterior wall of the trachea at the end. The inspired flow is unevenly distributed in subsequent bronchus by a cranial ridge at Cr20. The flow velocity profile is skewed on the right bronchus's upper side of the wall due to the bifurcation junction (Wang et al., 2009). The maximum velocity magnitude is observed at $t = 2.12$ s in both conditions. Similarly, the left airway has a high velocity magnitude, and it is attached to the bottom of the bronchus at $t = 2.12$ s. In contrast, flow is skewed in the upper side of the left bronchus (Adler and Brücker, 2007; Lin et al., 2007; Shang et al., 2019).



Cr- cross-section of marked location.

Figure 14. Tracheobronchial tree of HRT model.

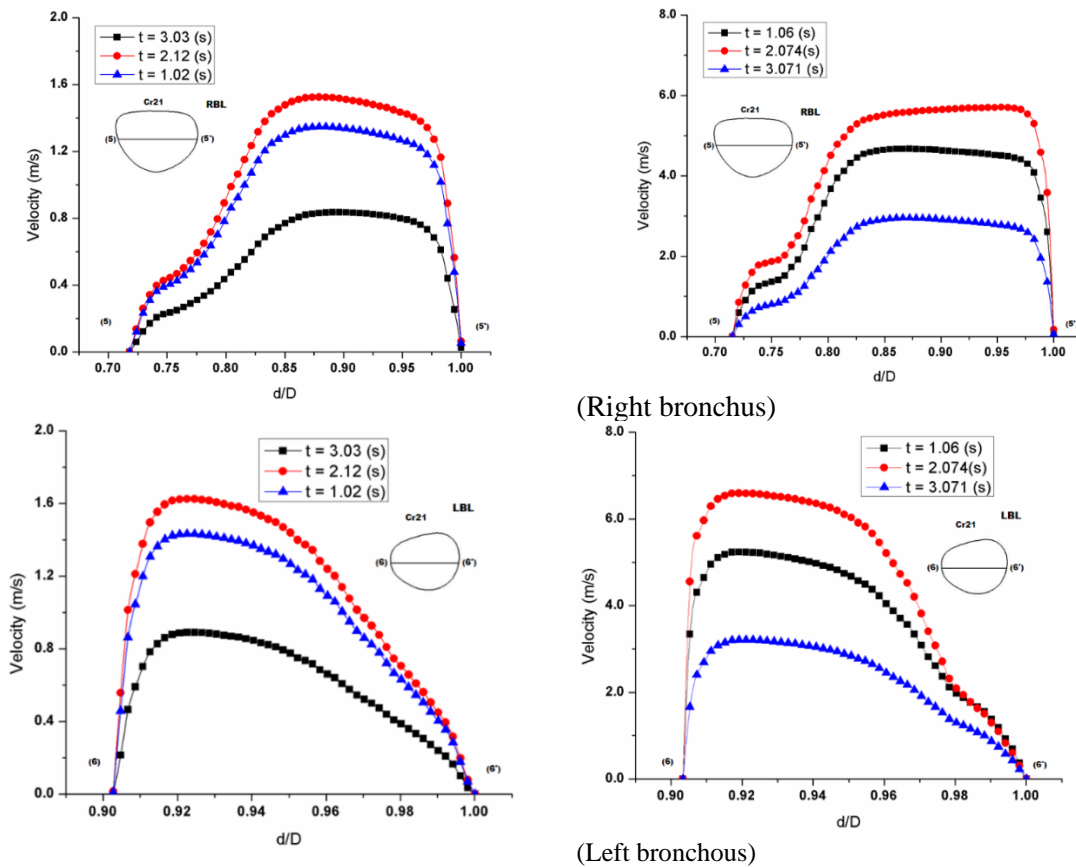


Figure 15. Mean velocity profile in the tracheobronchial airway, under the flow rate of, (a) 10 L/min, and (b) 40 L/min.

In Figure 16, flow velocity contours and secondary flow streamline in the right bronchus are presented in different cross-sections under normal and moderate inspiratory flow rates at different time steps.

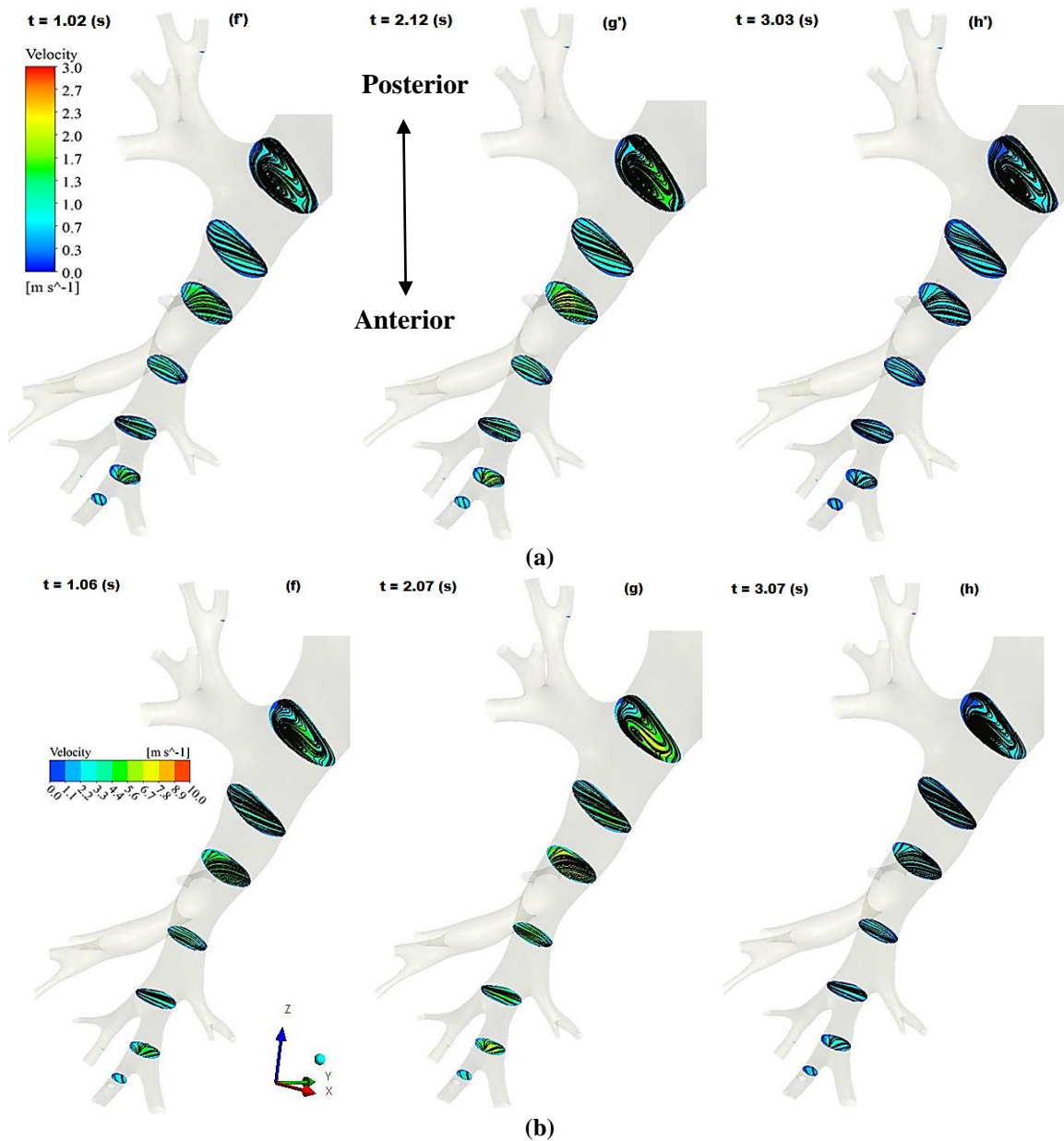


Figure 16. Secondary flow streamlines and velocity contours in the right bronchus under the flow rate of, (a) 10 L/min, and (b) 40 L/min.

It is evident from the zeroth junction (Cr20) in Figure 16 that the fully developed U shape velocity profile occurs at Cr20. However, Cr21 in the right bronchus airflow flow field in the bifurcation junction has high flow vortices due to curvature.

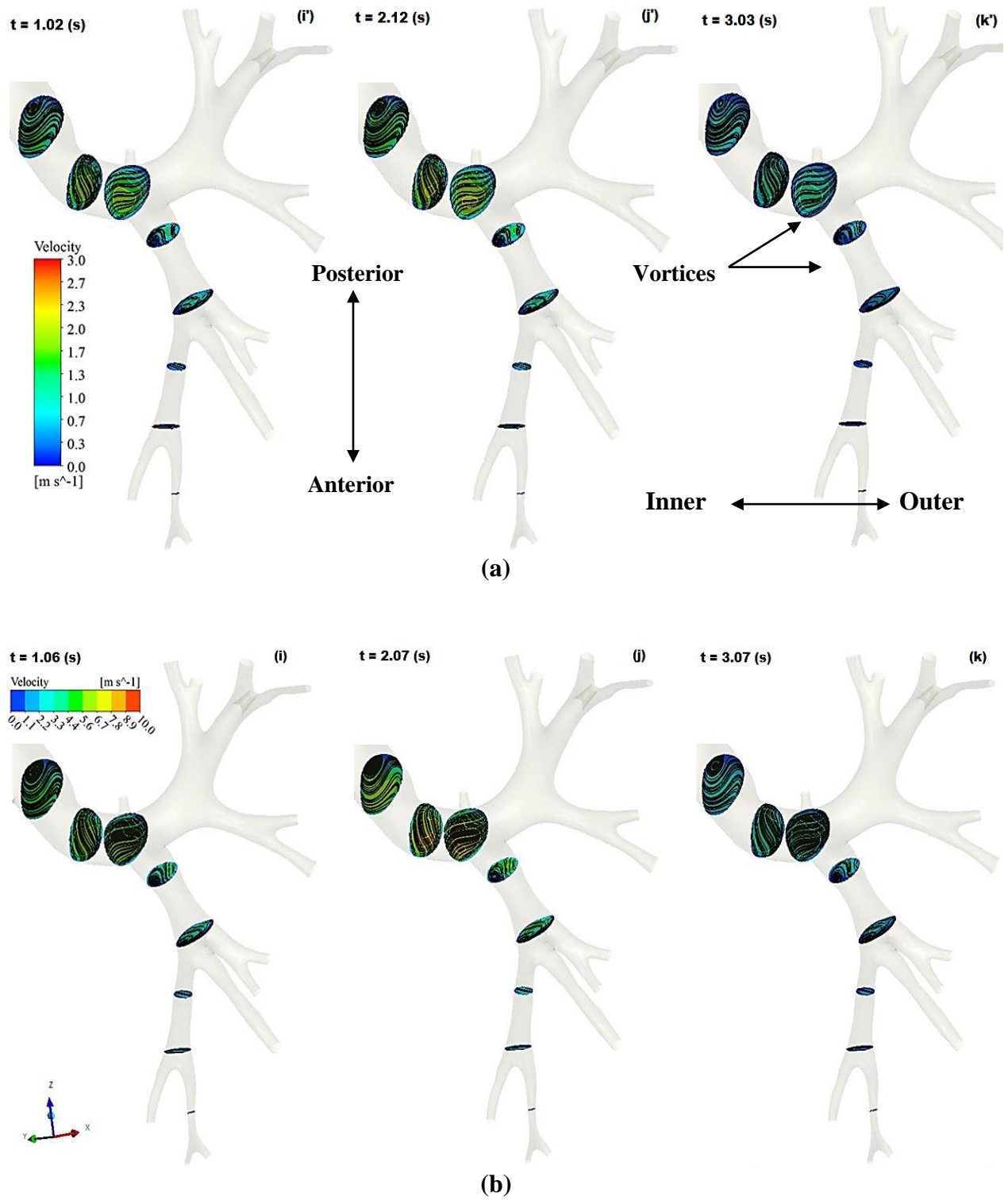


Figure 17. Secondary flow streamlines and velocity contours in the Left bronchus under the flow rate of, (a) 10 L/min, and (b) 40 L/min.

The maximum velocity magnitude ($t = 2.12$ s) is concentrated along the anterior side of the bronchus. While flow magnitude is reducing ($t = 3.03$ s) under low flow volume, The flow vortices remain attached to the anterior side, in contrast to the high inspiratory flow. The same results are seen at $t = 2.07$ s, as evident from Figures 16 (a) and (b) as the flow progressed in the subsequent daughter branches. The secondary flow vortices can be seen, and the flow magnitude gradually reduces in the lower airway.

Similarly, the detailed flow physics of the left bronchus is presented in Figures 17 (a) and (b). The inspired flow is entering the left primary bronchus. The secondary flow vortices have appeared along the posterior side of the wall. This is confirmed by the mean velocity profile at the cross-section Cr21 shown in Figure 15 in the left bronchus. The flow vortices are attached to the posterior side of the wall. The velocity magnitude is constructed in the middle region ($t = 2.12$ s). Thus, the flow patterns do not change under low flow volume ($t = 3.03$). The direction of flow vortices is followed in both bronchi. Due to anatomical structure, the maximum volume of air passes through the lower airway. The flow velocity magnitude is found to be along the outer side of the daughter bronchi, and vortices along the inner side are marked in Figure 17 (a) ($t = 2.21$ s).

The flow pattern is more sensitive in view of local characteristics under moderate flow, as shown in Figure 17(b). The two flow vortices are formed along the inner and outflow boundaries ($t = 2.07$ s). From Figure 17(b), the inner flow vortex shows dominance while reducing the flow rate ($t = 3.07$ s). The effect is still present, and the flow velocity magnitude is so small. Therefore, small flow vortices vanish on both sides of the airway.

3.4 Pressure Distribution in the Airways

In Figures 18 (a) and (b), the colour contours of pressure distribution at different time steps are presented in the HRT model. A significant pressure drop occurs in the upper airways in comparison to the tracheobronchial airways for flow in both conditions. In Figure 19, the pressure drop profile is calculated for both inspiratory inflow rates. During inhalation, a high-pressure drop (250 Pa) is identified ($t = 2.07$ s) under moderate inspiratory flow, as shown in Figure 19(b), as the flow passes from the pharynx and larynx regions.

A rapid pressure drop is observed. Due to the complex surface structure of the nasal cavity. Surface resistance is the primary factor in inspiratory flow (Shang et al., 2019). The glottis has a narrow cross-section, and the significant loss in pressure and high velocity magnitude are depicted. Due to its high velocity magnitude, the flow jet is constructed from the circle in Figure 18 ($t = 2.12$ s), which is evident from Figure 13. In the trachea, due to the circular cross-section, there is no significant change in pressure, as shown in Figures 19 (a) and (b), which is approximately a straight line.

The inspired flow volume of air is divided into the respective daughter tubes of the tracheobronchial tree. Therefore, every bifurcation junction of the right bronchus lung (RBL) and left bronchus lung (LBL) has a significant difference in pressure drop, as shown in Figures 20 (a) and (b). It is evident from the mean pressure profiles. The LBL has a higher pressure drop in (a and b). Furthermore, LBL has a higher pressure drop than RBL and is progressively increasing in lower bifurcation junctions. Despite the geometrical model limitations, pressure drop results are valid for the 7th bifurcation junction model.

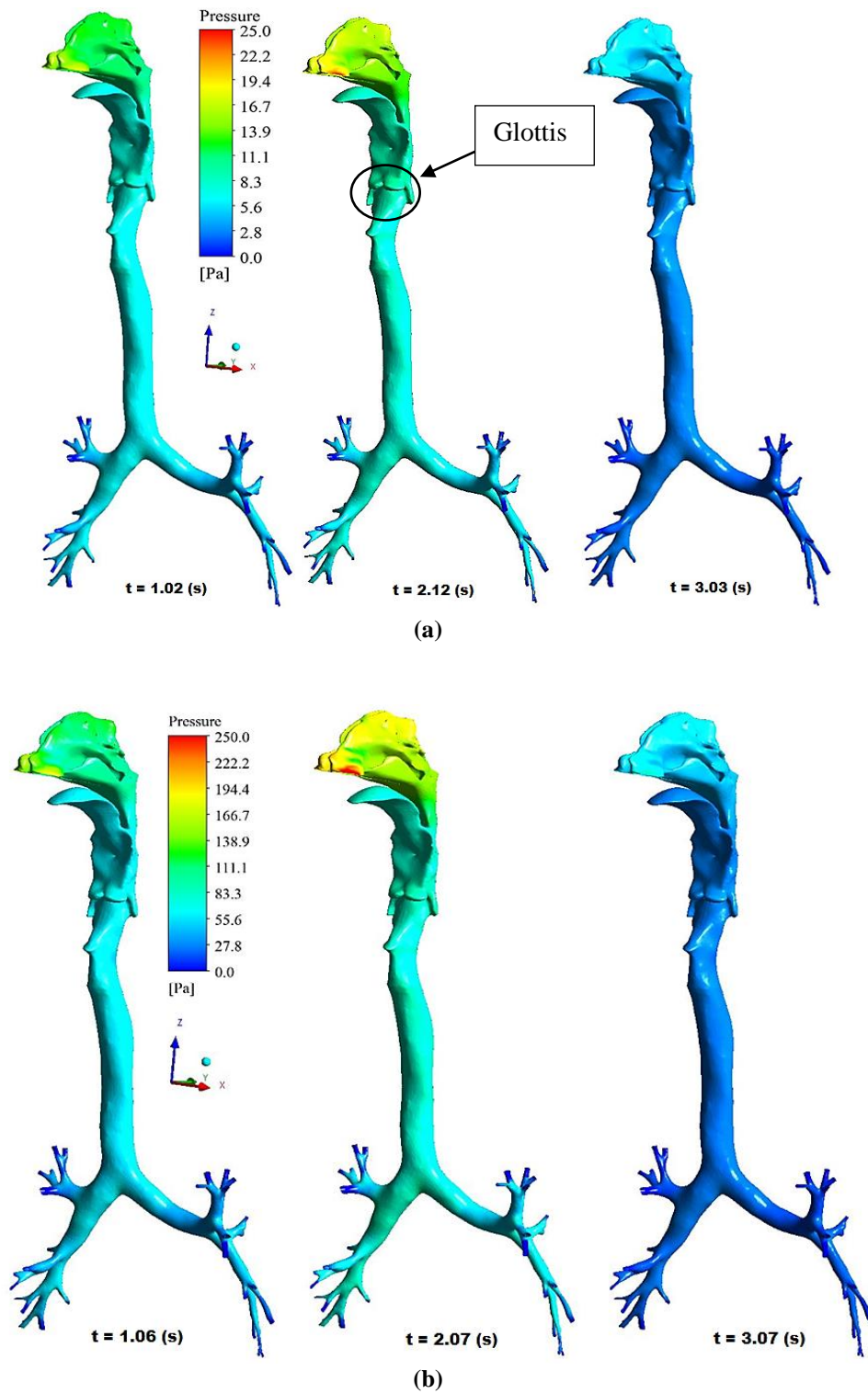


Figure 18. Static pressure distribution within the human airways under the flow rate of, (a) 10 L/min, and (b) 40 L/min.

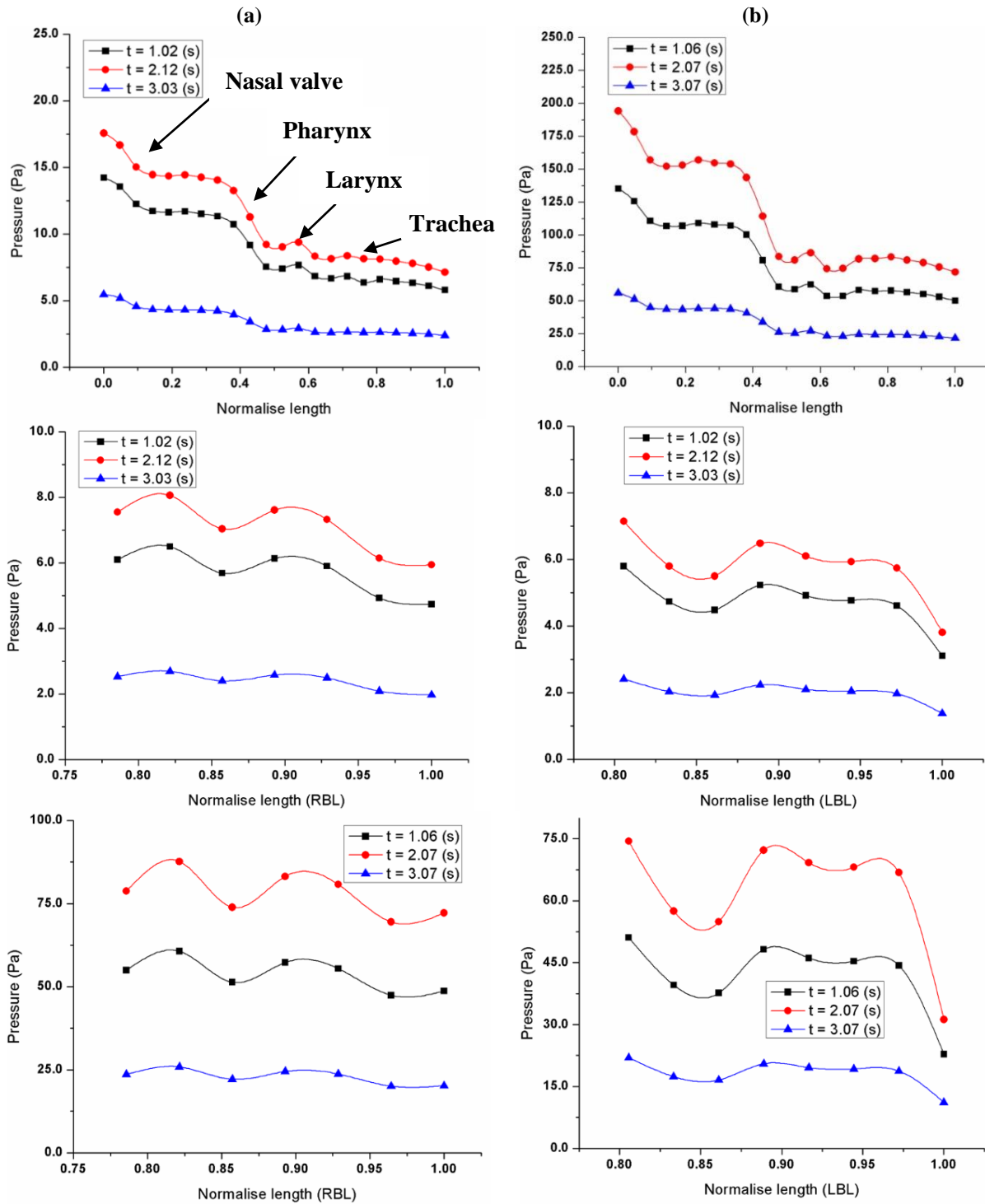


Figure 19. Mean static pressure distribution in the human airways at different time steps under the flow rate of, (a) 10 L/min, and (b) 40 L/min.

3.5 Particles Transport Patterns

The transport patterns of micro-sized particles (2.5 microns in diameter) in the HRT model are shown in Figures 20 (a) and (b) ($t = 1.02$ s, 2.12 s, and 3.02 s) under light and moderate inspiratory flow. Flow inertia and anatomical structure affect the transport pattern of particles in the HRT model. Therefore, to characterize these parameter effects on particles with asymmetric flow is essential. It is assumed that during expiratory flow The deposited particles are not exhaled because of the low velocity magnitude and flow vortices.

As the inspired flow accelerates, the micron-size particles are deposited on the distinct segments of the HRT model due to cross-section area variation and inertial impaction (I_p). Therefore, the transport pattern is analysed at the peak inspiratory flow ($t = 2.12$ s). The majority of particles are trapped in the nasal cavity of the vestibule region due to the narrow wall. The left nostril particle pattern differs from the right nostril due to the asymmetry of flow.

Under moderate flow, as shown in Figure 20(b), the transport pattern of particles changes significantly. It is evident from Figure 20 (b) ($t = 2.07$ s). Thus, the particles' total deposition fraction (TDF) is increased in the upper airways. Furthermore, flow progresses towards the nasal valve and respiration region. Due to the contraction of the cross-sectional area of the nasal valve, particles are passed through the middle meatus with the maximum magnitude of velocity. If the flow velocity is reduced, the concentrated mass of particles deposited at the inferior turbinate or bottom of the nasal cavity is shown in Figure 20(a, and b) ($t = 3.02$ s). Also, under low velocity, the magnitude of flow is found in the olfactory region, and flow vortices have appeared. Which affected the particle deposition.

The nasal cavity's respiration region (middle region) has a thick mucus and cilia layer, which can trap the inspired particles. Therefore, significant differences are found under light and moderate inspiratory flow. The flow streams of respective nostrils are merged in the nasopharynx region and travel towards the lower airways as a single stream. Due to the sudden proximal bend of the nasopharynx region, the particles get accelerated. It is seen in Figure 20 that the proximal deposition occurred at the pharynx and larynx region (marked from the circle).

The laryngeal flow is a high-flow vortex, so particles' deposition is increased in the pharynx and larynx regions. Also, due to flow, jet particles are concentrated in the middle of the glottis due to the nozzle effect mark in Figure 20(a) ($t = 2.12$ s). Therefore, particles tend to move towards the anterior side of the airway at peak inspiratory flow. At the entry of the trachea, a U-shaped velocity profile is presented due to the circular cross-section area (Adler and Brücker, 2007). The CT-scan-based HRT model has cartilage rings at the trachea that affect the local transport pattern of particles. These particles are non-uniformly striking onto the cranial ridge of the trachea, partitioned by the particles in the left and right main bronchi of HRT. However, the inertia of inspired particles is a primary mechanism for penetrating the particles in subsequent branches of the lungs. At the entry of the trachea, the particles are influenced by the inertia due to the glottis nozzle effect and airway bend.

Additionally, the flow development in the trachea prominently affects the concentration of the particles. As a result, more particles are shifted towards the right main bronchus instead of the left. Moreover, a low flow velocity zone is formed at the first bifurcation junction of the right bronchus, as seen in Figure 16, so the higher mass of particles is transported towards the left bronchus. Therefore, the results reveal that the total deposition fraction is higher in the left bronchus.

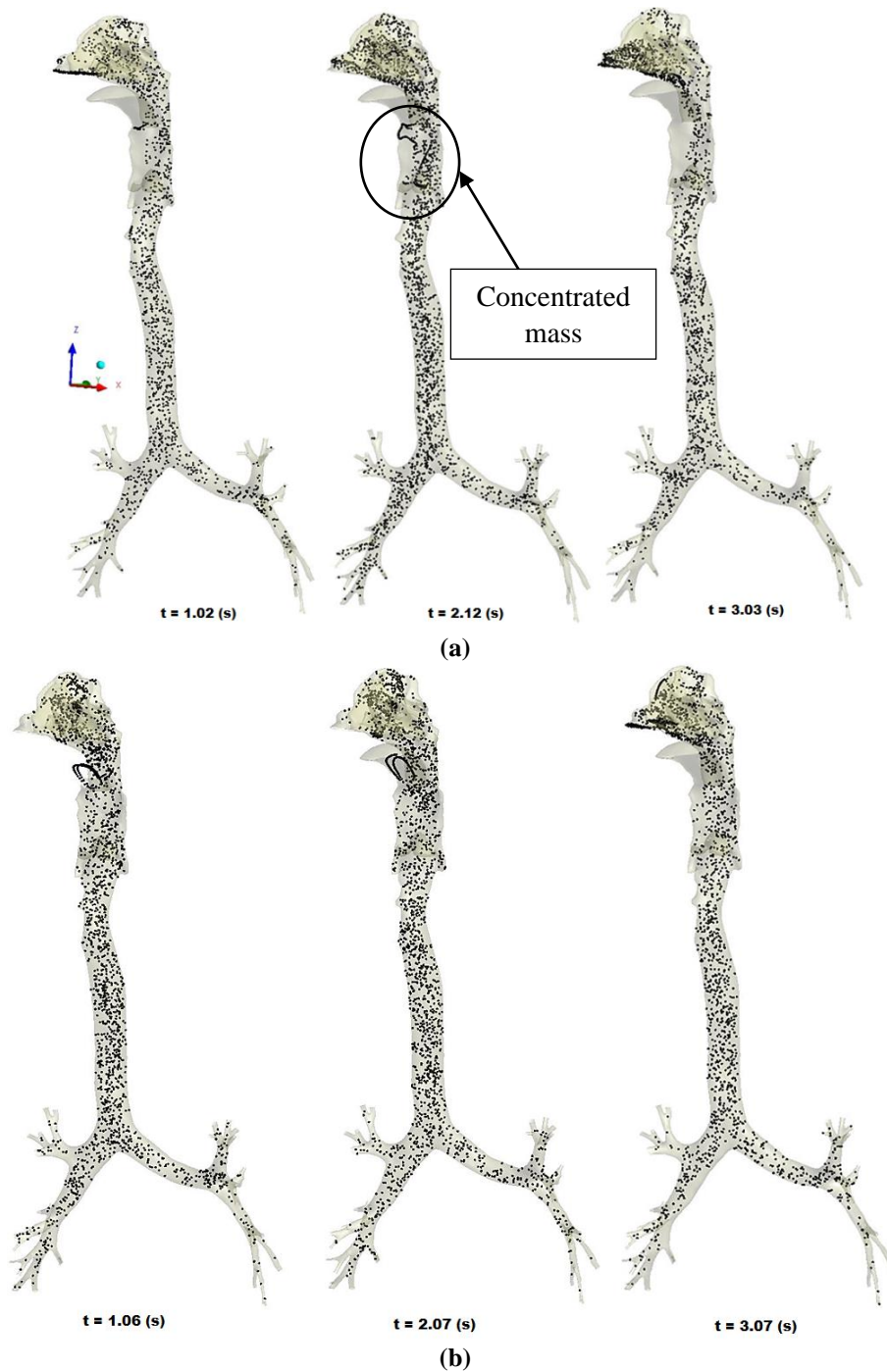


Figure 20. PM_{2.5} particles deposition pattern during natural inspiratory airflow in the human airways at different time steps under the flow rate of, (a) 10 L/min, and (b) 40 L/min.

3.6 Regional Deposition Fraction

Figures 21(a) and (b) present the regional deposition fraction of micro-sized particles. The total deposition fraction of micro-size particles is analyzed separately in upper airway regions such as the nasal

cavity, pharynx, larynx, and trachea. Also, the results of both cases are compared. The regional deposition fraction is defined as the ratio of the number of particles deposited in a particular region to the total number of particles inhaled.

During inhalation, the particles reach the flow wall with negligible velocity. Therefore, it can be trapped and deposited on the wall due to the mucosa and epithelial layer, which have tiny hairs called cilia. Under the poor AQI of $2.5 \mu\text{m}$, particle deposition in upper airways at two different inspiratory flow rates is compared in Figures 21(a) and (b). It is evident that the total deposition fraction (TDF) in the nasal cavity increases at a high flow rate due to the impaction ($d2Q$) of micro-sized particles under natural breathing. For $2.5 \mu\text{m}$ particles, TDF is marginally higher in a nasal cavity under moderated inspiratory flow ($t = 2.07 \text{ s}$). However, the $2.5 \mu\text{m}$ particle deposition increases in the pharynx and larynx regions under a moderate flow rate. As anticipated, the total deposition fraction for finer particles is not increased under moderate inspiratory flow.

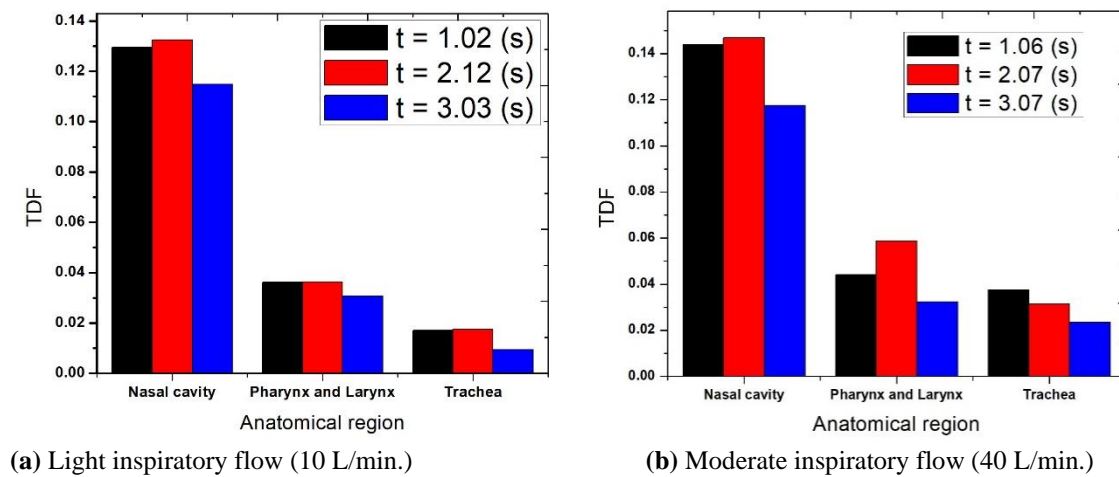


Figure 21. Regional total deposition fraction (TDF) of $2.5 \mu\text{m}$ particles in the upper airways.

In Figure 22(c and d), the deposition fraction of $2.5 \mu\text{m}$ particles in the left main bronchus bifurcation junctions is presented under light and moderate inspiratory flow. It is observed that the deposition fraction is decreasing from GEN-1 to GEN-7. The significant deposition fraction is obtained until the conductive junction of GEN-5; after that, TDF is reduced in subsequent bifurcation junctions. However, small numbers of particles cross the conductive junction; apart from that, the maximum number of particles are deposited in previous-generation bronchi. However, under moderated breathing, shown in Figure 22(d), no significant deposition fraction increased under the high flow rate.

Similarly, in Figure 22 (c' and d'), the TDF deposition in the bifurcation junctions of the right main bronchus is presented. A similar pattern of deposition fraction is obtained as received in the left bronchus. The particle deposition fraction is decreased continuously in the subsequent junction for $2.5 \mu\text{m}$ particle size. In order to lighten breathing, $\text{PM}_{2.5}$ deposition is not increased under moderate inspiratory flow. A higher deposition fraction is expected to be obtained from the right bronchus conductive zone. This is the character of the anatomical structure of transbronchial airways, which is more straight than the trachea. The available differences in the TDF pattern of the left and right main bronchus occur due to asymmetry in the respiratory tract structure and flow rate.

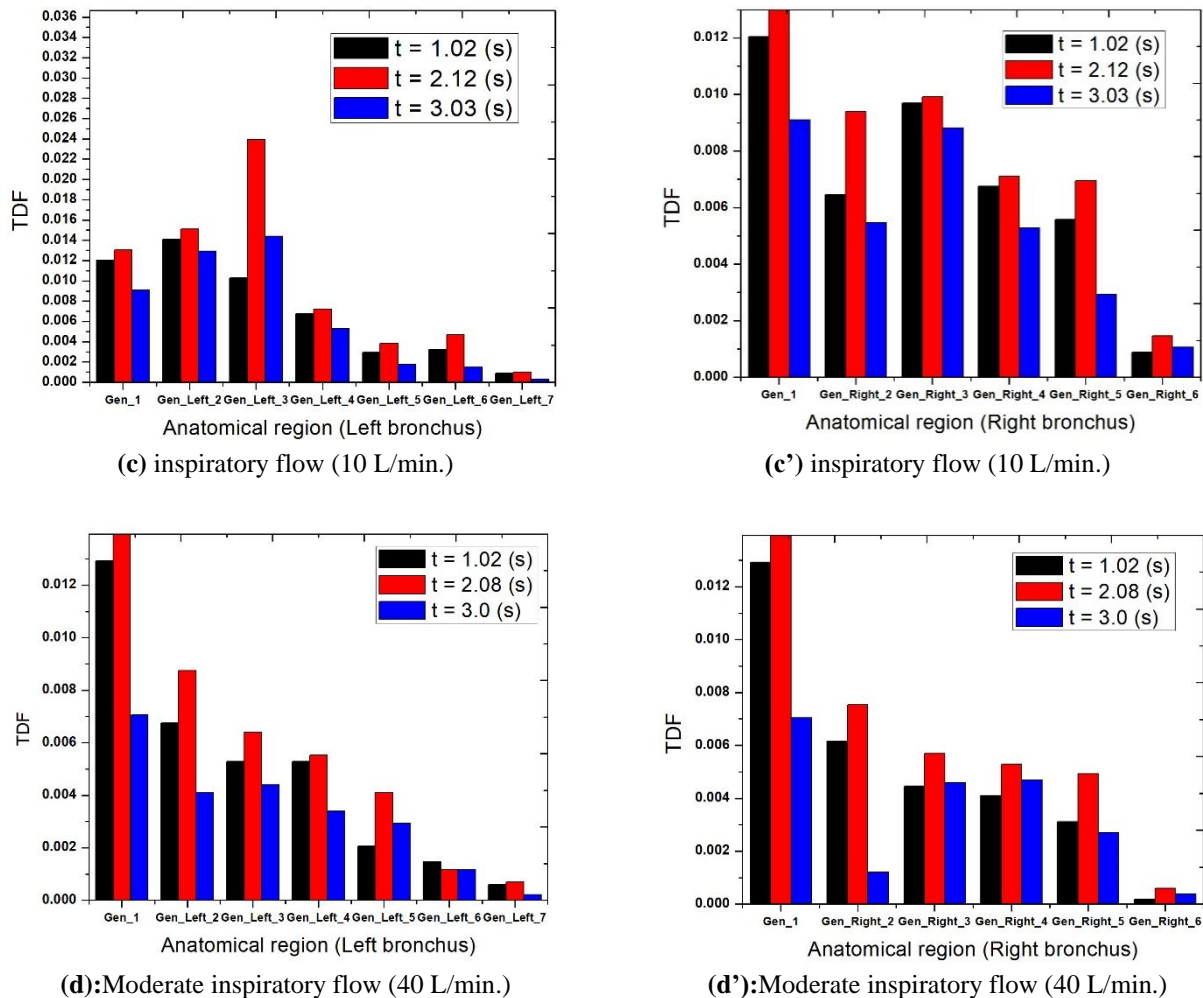


Figure 22. Total deposition fraction (TDF) of 2.5 μm particles in the left and right bronchus.

4. Conclusions

The primary facts and observations are reported as follows.

- (i) The asymmetry in nasal cavity flow is observed, and the left nostril has a higher flow magnitude than the right nostril.
- (ii) The higher flow vortices are found in the right nasal cavity and upper turbinate region under moderate breathing, which can increase a sense of smell and particle deposition.
- (iii) The local characteristics of respiration are more sensitive to the flow rates and anatomical structure. The flow vortices are found in the pharynx and larynx region.
- (iv) The flow vortex shows more dominance while reducing the flow rate at the bifurcation junctions. The effect is still present in daughter tubes. At the low magnitude of the flow, the flow vortices disappear on both sides of the daughter tubes.
- (v) A significant pressure drop occurs in the upper airway compared to the lower airways. The left bronchus shows a higher pressure drop than the right bronchus and progressively increases in lower bifurcation junctions. Despite the geometrical model limitations, these pressure drop results are valid up to 7th bifurcation junction.

- (vi) During natural respiration, the higher mass of particles are transported towards the left bronchus instead of the right bronchus. Therefore, high TDF is found in the left bronchus.
- (vii) The TDF for finer particles is not increased under moderate inspiratory flow. The significant deposition fraction is obtained until the conductive junction (GEN-5), after that TDF is reduced in subsequent bifurcation junctions. There is no significant change noticed in TDF under a moderate flow rate. The available differences in TDF pattern of the left and right main bronchus are found due to asymmetric flow and complex structure of airways.
- (viii) In future, for more clinical understanding of the particle deposition in the HRT model FSI (fluid-structure interaction) study must be considered.

Conflict of Interest

The authors declared this article has no conflict of interest.

Acknowledgements

This work was supported by the project on Effects of Respirable Suspended Particulate Matter (RSPM) on Chronic Obstructive Pulmonary Diseases (COPD) Using Computational Fluid Dynamics (CFD) sanctioned by the Council of Science and Technology, Government of Uttar Pradesh (India) vide sanction letter no.CST/ECT/D-268, dated May 14, 2015.

References

- Adler, K., & Brücker, C. (2007). Dynamic flow in a realistic model of the upper human lung airways. *Experiments in Fluids*, 43(2-3), 411-423.
- Ansys fluent guide (2016).
- Banko, A.J., Coletti, F., Elkins, C.J., & Eaton, J.K. (2016). Oscillatory flow in the human airways from the mouth through several bronchial generations. *International Journal of Heat and Fluid Flow*, 61, 45-57.
- Calmet, H., Houzeaux, G., Vázquez, M., Eguzkitza, B., Gambaruto, A.M., Bates, A.J., & Doorly, D.J. (2018). Flow features and micro-particle deposition in a human respiratory system during sniffing. *Journal of Aerosol Science*, 123, 171-184.
- Comer, J.K., Kleinstreuer, C., Hyun, S., & Kim, C.S. (2000). Aerosol transport and deposition in sequentially bifurcating airways. *Journal of Biomechanical Engineering* 122(2), 152-158.
- Deng, Q., Ou, C., Shen, Y.M., Xiang, Y., Miao, Y., & Li, Y. (2019). Health effects of physical activity as predicted by particle deposition in the human respiratory tract. *Science of the Total Environment*, 657, 819-826.
- Feng, Y., Zhao, J., Kleinstreuer, C., Wang, Q., Wang, J., Wu, D.H., & Lin, J. (2018). An in silico inter-subject variability study of extra-thoracic morphology effects on inhaled particle transport and deposition. *Journal of Aerosol Science*, 123, 185-207.
- Gorji, M.R., Pourmehran, O., Bandpy, M.G., & Gorji, T.B. (2015). CFD simulation of airflow behavior and particle transport and deposition in different breathing conditions through the realistic model of human airways. *Journal of Molecular Liquids*, 209, 121-133.
- Huang, F., Zhang, Y., Tong, Z.B., Chen, X.L., Yang, R.Y., & Yu, A.B. (2021). Numerical investigation of deposition mechanism in three mouth–throat models. *Powder Technology*, 378, 724-735.
- Hughes, B.B., Kuhn, R., Rothman, D.S., & Solórzano, J.R. (2011). Patterns of potential human progress. *Paradigm Publishers and Oxford University Press India*, 3, 1-20.
- Inthavong, K., Chetty, A., Shang, Y., & Tu, J. (2018). Examining mesh independence for flow dynamics in the human nasal cavity. *Computers in Biology and Medicine*, 102, 40-50.

- Inthavong, K., Ma, J., Shang, Y., Dong, J., Chetty, A.S., Tu, J., & Frank-Ito, D. (2019). Geometry and airflow dynamics analysis in the nasal cavity during inhalation. *Clinical Biomechanics*, 66, 97-106.
- Kang, M.Y., Hwang, J., & Lee, J.W. (2011). Effect of geometric variations on pressure loss for a model bifurcation of the human lung airway. *Journal of Biomechanics*, 44(6), 1196-1199.
- Kelly, J.T., Asgharian, B., Kimbell, J.S., & Wong, B.A. (2004). Particle deposition in human nasal airway replicas manufactured by different methods. Part I: Inertial regime particles. *Aerosol Science and Technology*, 38(11), 1063-1071.
- Keyhani, K., Scherer, P.W., & Mozell, M.M. (1995). Numerical simulation of airflow in the human nasal cavity. *Journal of Biomechanical Engineering*, 117(4), 429-441.
- Kim, S., & Lee, S.J. (2007). Measurement of 3D laminar flow inside a micro tube using micro digital holographic particle tracking velocimetry. *Journal of Micromechanics and Microengineering*, 17(10), 2157-2162.
- Kleinstreuer, C., & Zhang, Z. (2002). Targeted drug aerosol deposition analysis for a four-generation lung airway model with hemispherical tumors. *Journal of Biomechanical Engineering*, 125(2), 197-206.
- Lee, J.H., Na, Y., Kim, S.K., & Chung, S.K. (2010). Unsteady flow characteristics through a human nasal airway. *Respiratory Physiology & Neurobiology*, 172(3), 136-146.
- Lin, C.L., Tawhai, M.H., McLennan, G., & Hoffman, E.A. (2007). Characteristics of the turbulent laryngeal jet and its effect on airflow in the human intra-thoracic airways. *Respiratory Physiology & Neurobiology*, 157(2-3), 295-309.
- Liu, Z., Hu, B., Ji, D., Wang, Y., Wang, M., & Wang, Y. (2015). Diurnal and seasonal variation of the PM_{2.5} apparent particle density in Beijing, China. *Atmospheric Environment*, 120, 328-338.
- Lopez, A.D., & Mathers, C.D. (2006). Measuring the global burden of disease and epidemiological transitions: 2002-2030. *Annals of Tropical Medicine & Parasitology*, 100, 481-499.
- Luo, H.Y., & Liu, Y. (2009). Particle deposition in a CT-scanned human lung airway. *Journal of Biomechanics*, 42(12), 1869-1876.
- Luo, H.Y., & Liu, Y. (2009). Particle deposition in a CT-scanned human lung airway. *Journal of Biomechanics*, 42(12), 1869-1876.
- Luo, X.Y., Hinton, J.S., Liew, T.T., & Tan, K.K. (2004). LES modelling of flow in a simple airway model. *Medical Engineering & Physics*, 26(5), 403-413.
- Ma, J., Dong, J., Shang, Y., Inthavong, K., Tu, J., & Frank-Ito, D.O. (2018). Air conditioning analysis among human nasal passages with anterior anatomical variations. *Medical Engineering & Physics*, 57, 19-28.
- Mathers, C.D., & Loncar, D. (2006). Projections of global mortality and burden of disease from 2002 to 2030. *PLoS Medicine*, 3(11), 1-20.
- Morsi, A.J., & Alexander, S.A. (1972) An investigation of particle trajectories in two-phase flow system. *Journal of Fluid Mechanics*, 55, 193-208.
- Mutuku, J.K., & Chen, W.H. (2018). Flow characterization in healthy airways and airways with chronic obstructive pulmonary disease (COPD) during different inhalation conditions. *Aerosol and Air Quality Research*, 18(10), 2680-2694.
- Naseri, A., Shaghaghian, S., Abouali, O., & Ahmadi, G. (2017). Numerical investigation of transient transport and deposition of microparticles under unsteady inspiratory flow in human upper airways. *Respiratory Physiology & Neurobiology*, 244, 56-72.
- Piemjaiswang, R., Shiratori, S., Chaiwatanarat, T., Piumsomboon, P., & Chalermssinsuwan, B. (2019). Computational fluid dynamics simulation of full breathing cycle for aerosol deposition in trachea: Effect of breathing frequency. *Journal of the Taiwan Institute of Chemical Engineers*, 97, 66-79.

- Piglione, M.C., Fontana, D., & Vanni, M. (2012). Simulation of particle deposition in human central airways. *European Journal of Mechanics-B/Fluids*, 31, 91-101.
- Pirhadi, M., Sajadi, B., Ahmadi, G., & Malekian, D. (2018). Phase change and deposition of inhaled droplets in the human nasal cavity under cyclic inspiratory airflow. *Journal of Aerosol Science*, 118, 64-81.
- Riazuddin, V.N., Zubair, M., Abdullah, M.Z., Ismail, R., Shuaib, I.L., Hamid, S.A., & Ahmad, K.A. (2011). Numerical study of inspiratory and expiratory flow in a human nasal cavity. *Journal of Medical and Biological Engineering*, 31(3), 201-206.
- Salim, S.M., & Cheah, S. (2009). Wall Y strategy for dealing with wall-bounded turbulent flows. In *Proceedings of the International Multiconference of Engineers and Computer Scientists*, 2, 2165-2170.
- Schroeter, J.D., Garcia, G.J., & Kimbell, J.S. (2011). Effects of surface smoothness on inertial particle deposition in human nasal models. *Journal of Aerosol Science*, 42(1), 52-63.
- Shang, Y., Dong, J., Tian, L., Inthavong, K., & Tu, J. (2019). Detailed computational analysis of flow dynamics in an extended respiratory airway model. *Clinical Biomechanics*, 61, 105-111.
- Singh, D. (2021). Numerical assessment of natural respiration and particles deposition in the computed tomography scan airway with a glomus tumour. *Proceedings of the Institution of Mechanical Engineers, Part E: Journal of Process Mechanical Engineering*, 235(6), 1945-1956.
- Singh, D., Jain, A., & Paul, A.R. (2022). Numerical assessment of a 3D human upper respiratory tract model: effect of anatomical structure on asymmetric tidal pulmonary ventilation characteristics. *International Journal of Biomedical Engineering and Technology*, 38(3), 225-248.
- Soni, B., & Aliabadi, S. (2013). Large-scale CFD simulations of airflow and particle deposition in lung airway. *Computers & Fluids*, 88, 804-812.
- Spiegel, D., Loewenstein, R.J., Lewis-Fernández, R., Sar, V., Simeon, D., Vermetten, E., & Dell, P.F. (2011). Dissociative disorders in DSM-5. *Depression and Anxiety*, 28(12), 17-45.
- Srivastav, V.K., Kumar, A., Shukla, S.K., Paul, A.R., Bhatt, A.D., & Jain, A. (2014). Airflow and aerosol-drug delivery in a CT scan based human respiratory tract with tumor using CFD. *Journal of Applied Fluid Mechanics*, 7(2), 345-356.
- Srivastav, V.K., Paul, A.R., & Jain, A. (2019). Capturing the wall turbulence in CFD simulation of human respiratory tract. *Mathematics and Computers in Simulation*, 160, 23-38.
- Sul, B., Wallqvist, A., Morris, M.J., Reifman, J., & Rakesh, V. (2014). A computational study of the respiratory airflow characteristics in normal and obstructed human airways. *Computers in Biology and Medicine*, 52, 130-143.
- Tanprasert, S., Kampeewichean, C., Shiratori, S., Piemjaiswang, R., & Chalermssinsuwan, B. (2023). Non-spherical drug particle deposition in human airway using computational fluid dynamics and discrete element method. *International Journal of Pharmaceutics*, 639, 122979.
- Wang, Y., Liu, Y., Sun, X., Yu, S., & Gao, F. (2009). Numerical analysis of respiratory flow patterns within human upper airway. *Acta Mechanica Sinica*, 25(6), 737-746.
- Weinhold, I., & Mlynski, G. (2004). Numerical simulation of airflow in the human nose. *European Archives of Oto-Rhino-Laryngology and Head & Neck*, 261, 452-455.
- Wen, J., Inthavong, K., Tu, J., & Wang, S. (2008). Numerical simulations for detailed airflow dynamics in a human nasal cavity. *Respiratory Physiology & Neurobiology*, 161(2), 125-135.
- Yang, X.L., Liu, Y., & Luo, H.Y. (2006). Respiratory flow in obstructed airways. *Journal of Biomechanics*, 39(15), 2743-2751.

- Zhang, Z., & Kleinstreuer, C. (2002). Transient airflow structures and particle transport in a sequentially branching lung airway model. *Physics of Fluids*, 14(2), 862-880.
- Zhang, Z., Kleinstreuer, C., & Kim, C.S. (2001). Flow structure and particle transport in a triple bifurcation airway model. *Journal of Fluids Engineering*, 123(2), 320-330.
- Zhu, Z., Zhang, C., & Zhang, L. (2019). Experimental and numerical investigation on inspiration and expiration flows in a three-generation human lung airway model at two flow rates. *Respiratory Physiology & Neurobiology*, 262, 40-48.



Original content of this work is copyright © International Journal of Mathematical, Engineering and Management Sciences. Uses under the Creative Commons Attribution 4.0 International (CC BY 4.0) license at <https://creativecommons.org/licenses/by/4.0/>

Publisher's Note- Ram Arti Publishers remains neutral regarding jurisdictional claims in published maps and institutional affiliations.